Effect of the deposition direction on fracture propagation in a Duplex Stainless Steel manufactured by Directed Energy Deposition

David Roucou, Thomas Corre, Gilles Rolland, Véronique Lazarus

Effect of the deposition direction on fracture propagation in a Duplex Stainless Steel manufactured by Directed Energy Deposition

David Roucou[a,*], Thomas Corre[a,b], Gilles Rolland[a,c] and Véronique Lazarus[a]

[a]IMSIA, CNRS, EDF, CEA, ENSTA Paris, Institut Polytechnique de Paris, 91120 Palaiseau Cedex, France
[b]Nantes Université, Ecole Centrale Nantes, CNRS, GeM, UMR 6183, F-44000 Nantes, France
[c]MMC, EDF R&D, Les Renardières, France

ARTICLE INFO

Keywords:
Directed energy deposition
Duplex stainless steel
Fracture anisotropy

ABSTRACT

Dense volumes of duplex stainless steel are manufactured by directed energy deposition. Compact tension specimens are machined from these volumes in order to evaluate the fracture toughness in two directions : parallel or perpendicular to the deposited layers. Different values are measured in the two cases. In order to understand this anisotropy, additional analyzes are performed on the cracked specimens post-mortem. A classical metallography analysis reveals the highly oriented structure of the material, as well as phase localization. The study of the fracture surface reveals several points. At the macroscale, while the crack surfaces are flat in the parallel case, pronounced shear lips cover half of the fracture surface in the perpendicular case. At the microscale, fracture is ruled by microvoid coalescence. The mesoscale, which is inherited from the deposition strategy, is found to pilot the crack growth. The border between the primary solidified melt pools and the heat-affected zones, which corresponds to the interface between the deposited layers, is the preferred area for crack growth. Analyzing the crack surface roughness confirms the dominance of the mesoscale, as its characteristic lengthscale is retrieved. This explains the differences observed for the two tested directions of fracture: in the parallel case, the crack is aligned with the weak interfaces between layers, which channel the crack growth; in the orthogonal one, out-of-plane excursion of the crack becomes possible allowing the crack to follow a tortuous three-dimensional path that results in a higher toughness than in the parallel situation.

1. Introduction

Duplex stainless steels (DSS) offer good corrosion resistance and mechanical properties, and are thus materials of choice in specific environments. These properties are conferred by their particular biphasic microstructure, made of ferrite and austenite mostly. Wrought DSS are usually adjusted to a composition of approximately 50 % of each phase, where the best combination of properties is reached [25, 15].

Additive manufacturing (AM) has recently been a topic of particular research interest, notably for the elaboration of metallic components [24, 12]. Progress in this field has allowed to process dense metallic parts with properties as good as -or even better than- with conventional methods [16]. Therefore AM, which was formerly restrained to rapid prototyping, can be considered for more demanding manufacturing applications. Complex three-dimensional parts can be built, usually through layer-by-layer deposition. Among metallic AM processes, directed energy deposition (DED) is of particular interest as it could be used as a means to repair damaged parts directly. This process consists in using a concentrated energy source to melt a feedstock material, allowing its deposition on a substrate through controlled movements of the system [11]. In this study, the process uses powder projected through a mobile nozzle as feedstock material and a laser as an energy source.

Fracture properties of AM materials have to be assessed for those to be usable in practical applications. Due to the layer by layer deposition mode, they present specific microstructures which can induce a marked anisotropy in the fracture properties [20, 10]. In the case of metallic alloys, additional complexity arises from the fact that their microstructure and properties are highly dependent on the thermal history. Indeed, the repeated passes of the heat source

*Corresponding author
david.roucou@ensta-paris.fr (D. Roucou)
ORCID(s):

Fe	Cr	Ni	Mo	Mn	Si	N	Cu	C	P	S
Bal.	25.0	7.0	4.0	<1.2	<0.8	0.30	<0.5	<0.03	<0.035	<0.015

Table 1
Composition of the SAF2507 super DSS powder (wt%).

during the fabrication process induces local reheating that strongly depends on the deposition strategy, leading to a complex local thermal history. Such fabricated materials can be post-processed with heat treatments, which can modify the microstructure and the process-induced defects [34]. Fracture anisotropy of AM metals has been studied for various alloys [4], such as Ti-6Al-4V [8, 33, 21, 22], AlSi10Mg [13, 27], or steels [38, 23, 28]. Some studies have reported anisotropic fracture properties [8, 38, 33, 22, 13, 27, 28], but the opposite result is found in other studies [21, 28]. Therefore, different alloys manufactured with new processes should be tested as there appears to be no universal result. The material's micro- and meso-structures are generally studied to explain the fracture processes. Some authors have found that the heat-affected zones (HAZ), *i.e.* the regions which are reheated by the subsequent passing of the laser, can constitute a preferential region for fracture [13, 27]. AM of DSS is quite recent and is still under active research [41]. To date, there have been few published studies on these materials processed by DED [7, 17].

The present study aims to present experimental results on the fracture properties of a super DSS (*i.e.* third generation DSS) processed by DED. In particular, fracture anisotropy is assessed by performing fracture tests in two different orientations with regard to the as-built material. The DSS powder used, the DED fabrication procedure and the Compact Tension tests are presented in section 2. The results of these fracture tests are given in section 3: the material is found to have an isotropic apparent stiffness but anisotropic fracture toughness. The origin of this anisotropy is discussed in section 4 in correlation with metallographic and fractographic analyzes.

2. Materials and methods

2.1. Fabrication of the duplex stainless steel volumes

The feedstock material used in this study is the super DSS powder SAF2507 manufactured by Sandvik Osprey. The particle sizes range between 45 and 90 µm, and the composition, as indicated by the manufacturer, is reported in Table 1.

The DED machine used to realize the builds is the *Mobile* machine from BeAM, equipped with a 500W YLR-fiber laser. Additional information on the machine has been described by Balit et al. [1, 2]. Parallelepipedic volumes were elaborated in a single-step process (Figure 1, top left). These were made 45 mm tall in the building direction, with a base of dimensions 45 mm * 13 mm. This choice of dimensions allowed to machine all the specimens from the same initial raw geometry. No heat treatment or additional preparation step were applied before or after machining the specimens. Each layer was scanned using a raster strategy, which consists in back and forth movements of the nozzle as shown in Figure 1, bottom. An overlap of 35% between neighbouring tracks was aimed for, leading to a hatch spacing (*i.e.* the actual distance between the middles of each track) of 0.39 mm. The layer height was 0.2 mm. In order to help the description of the considered orientations, an axis system relative to the directions of fabrication of the volume has been defined as follows (Figure 1, top right) : the building direction (B) in which the layers are subsequently superposed, the longitudinal direction (L) which also corresponds to the direction of the deposited tracks, and the transverse direction (T). This axis system will be reused throughout the subsequent figures to specify the relevant orientations and the planes of interest. In particular, the layers belong to the (L-T) plane defined by the longitudinal and transverse direction vectors.

The displacement speed of the nozzle during the fabrication was set to 2000 mm/min, and the laser power was 250 W. The powder flow rate, measured by weighting the expulsed powder during a 2 minute test, was approximately 7 g/min.

2.2. Fracture tests

The fracture behavior of the material was tested using compact tension (CT) specimens. The dimensions were defined following the standard ISO 12135 [18] with the width parameter $W = 32$ mm (Figure 2, left). The volumes built as explained in §2.1 allowed to machine the initial notch in two directions : either parallel to the deposited tracks, or along the building direction (Figure 2, right). In the following, each specimen will be annotated with the "//" or

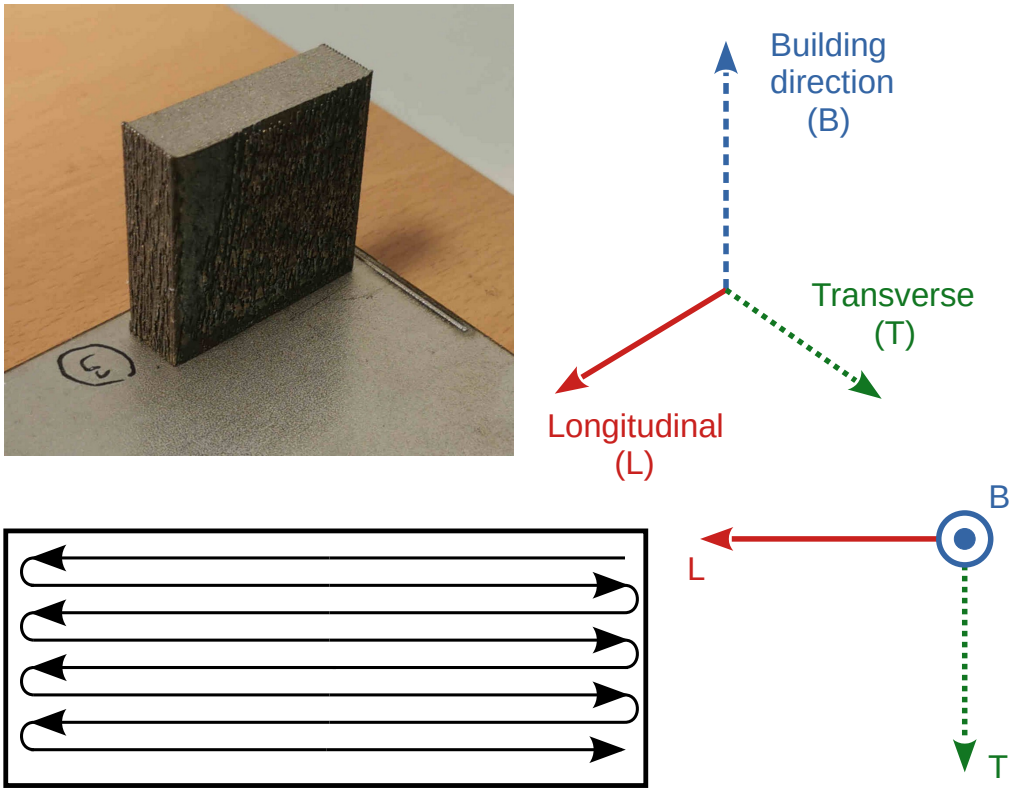

Figure 1: Raw built volume (top left), Associated axis system (top right), Layer deposition strategy (bottom).

"⊥" symbol accordingly. The total length of the machined notch was 20.5 mm. All the following procedures have been performed on an MTS 312 servo-hydraulic machine, equipped with a 100 kN capacity load cell.

First, the samples were cycled in fatigue to realise a precrack, aiming for a minimal length of 2 mm. The specimens were cycled under load control at a frequency of 10 Hz (sine wave) with a maximum load of $F_{max} = 6$ kN and a loading ratio $R = F_{min}/F_{max} = 0.1$. The total number of cycles was different for each specimen due to variability in crack initiation, and the cycles were made by steps of 10 000 cycles after which the crack length was assessed. The precracking procedure was stopped when the visible crack length was measured larger than 2 mm on both sides of the specimen. This choice of length respects the conditions imposed by ISO 12135 [18] regarding both the length of the precrack alone as well as the total combined length of the machined notch and the precrack.

Second, rupture tests were performed by imposing a monotonous displacement at a fixed crosshead speed of 0.2 mm/min. The controlled displacement was applied until a limit value of 5 mm was reached. At this point, the specimens were found to be partially cracked, and were removed for further analysis. It can be noted that the crack extension was stable during the whole test.

3. Results: anisotropy of the fracture toughness

Two specimens were tested for each orientation, *i.e.* with the notch either parallel (//) or orthogonal (⊥) to the deposited layers. Figure 3 shows the recorded loads versus load-line displacements. The two types of specimens present similar apparent stiffnesses in the elastic regime, while showing remarkably different behaviors during crack growth.

The specimens for the two orientations present different crack behaviors which can be observed on their outer surfaces. For the parallel orientation, the crack propagates in a straight manner (Figure 4, left). Small local deviations from the middle crack plane, which form small crenels, are observed. Nevertheless, the crack is broadly prolonging

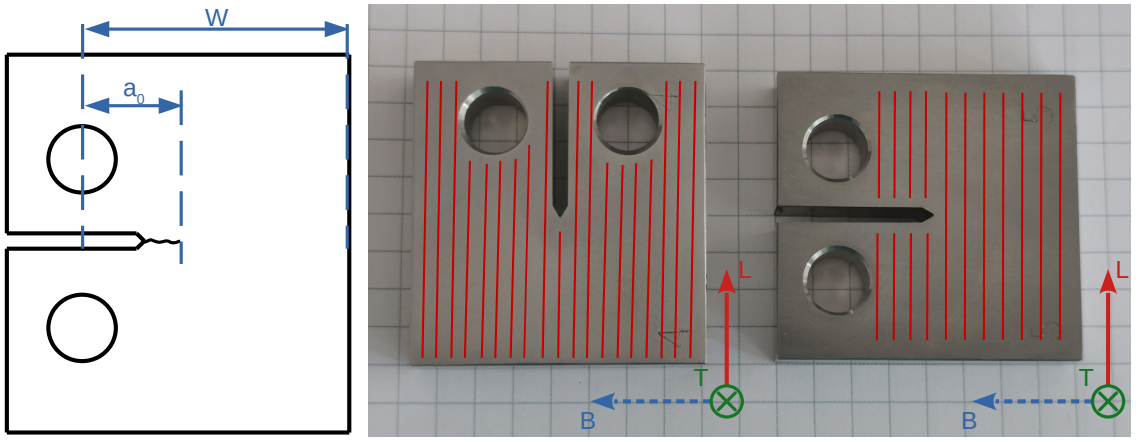

Figure 2: Illustration of a CT specimen (Left) and machining directions (Middle: // specimen, Right: ⊥ specimen). Red lines represent the orientations of the tracks.

the plane of the fatigue precrack, while for the second orientation a more complex crack pattern is observed (Figure 4, right). At crack initiation, a bifurcation of the crack into two branches is observed. Then, only one of them continues to propagate while the second branch remains small. This deflected crack pattern is accompanied by a non-flat crack surface throughout the thickness, which is further described in §4.2.1. These observations are identical for each pair of specimens.

All the CT specimens, which were partially cracked after the rupture test, have been fully opened by imposing a large displacement with the traction machine. The state of the specimen near the initial crack tip is well preserved, allowing to measure the length of the fatigue precrack. This was done by averaging six measurements made with a Keyence VHX-600 digital microscope throughout the specimen's thickness.

Following the standard ISO 12135 [18], the slope of the initial linear portion of the fracture tests was determined. Then, the secant with a slope equal to 95% of the linear region was drawn, and its intersection with the measured load-displacement curve defines the provisional load F_Q. This value is used to calculate the provisional value of the stress intensity factor K_Q, using the formula :

$$K_Q = \frac{F_Q}{B\sqrt{W}} \cdot g_2\left(\frac{a_0}{W}\right), \tag{1}$$

where B is the specimen thickness, W and a_0 are the width parameter and the initial crack length illustrated in Figure 2, and g_2 is the expression proposed by Srawley [36]:

$$\begin{aligned} g_2\left(\frac{a_0}{W}\right) = &\frac{\left(2+\frac{a_0}{W}\right)}{\left(1-\frac{a_0}{W}\right)^{1.5}}\left[\,0.886 + 4.64\frac{a_0}{W} - 13.32\left(\frac{a_0}{W}\right)^2\right. \\ &\left. +14.72\left(\frac{a_0}{W}\right)^3 - 5.6\left(\frac{a_0}{W}\right)^4\right] \end{aligned} \tag{2}$$

The relevant measures or calculated quantities for each test are presented in Table 2. The maximum loads measured for the ⊥ specimens were 27 kN on average, whereas their counterparts were 22 kN on average. Note that the specimen in the parallel direction labeled as 1// presented an initial precrack measured noticeably shorter than the other specimens, which likely explains the noticeable difference in measured loads (F_{max}, F_Q) for the two // specimens : the differences in a_0 and F_Q compensate each other and the K_Q values found are in agreement.

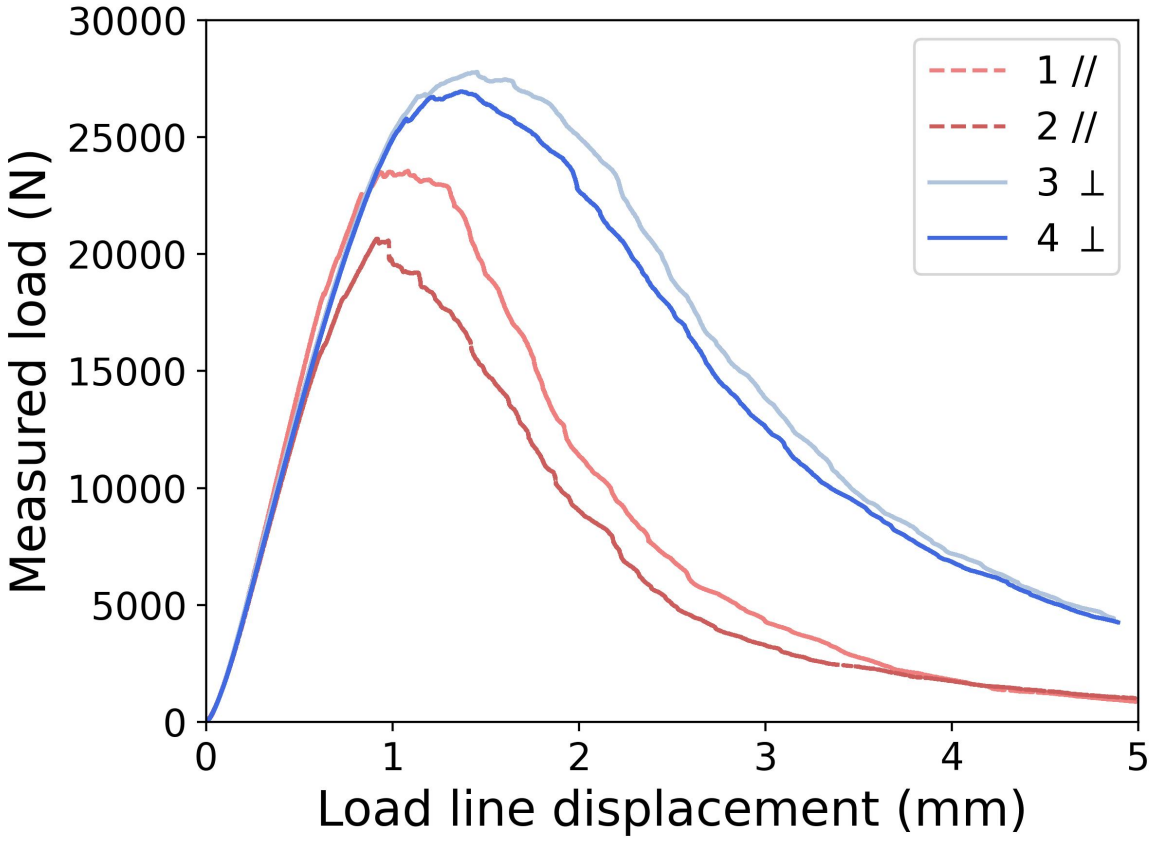

Figure 3: Measured load versus load line displacement curves for each CT specimen.

Specimen	a_0 (mm)	F_{max} (N)	F_Q (N)	K_Q (MPa.$\sqrt{m}$)
1//	13.9	23 556	19 807	88.41
2//	15.3	20 655	16 709	84.55
3⊥	15.14	27 791	22 245	110.81
4⊥	15.32	26 953	22 678	112.83

Table 2
Values obtained for relevant quantities of the fracture test for each specimen : Initial crack length a_0, maximum measured load F_{max}, provisional force value F_Q, provisional fracture toughness value K_Q.

According to ISO 12135 [18], these values do not pass the validity tests and thus cannot be considered to be K_{Ic} values. This is *a priori* due to the size of the plastic zone at the tip of the crack, which is non negligible compared to the other dimensions in play. Thus, the theory of linear elastic fracture mechanics does not properly apply to the considered problem. However, the specimen geometries were identical for both orientations. In addition to the fact that the elastic properties were found to be the same in both cases, the K_Q values obtained allow qualitative discussion on the material's fracture toughness with regard to the building direction. The values for the ⊥ specimens are found significantly higher than for the other direction, expressing a considerable fracture toughness anisotropy for this material.

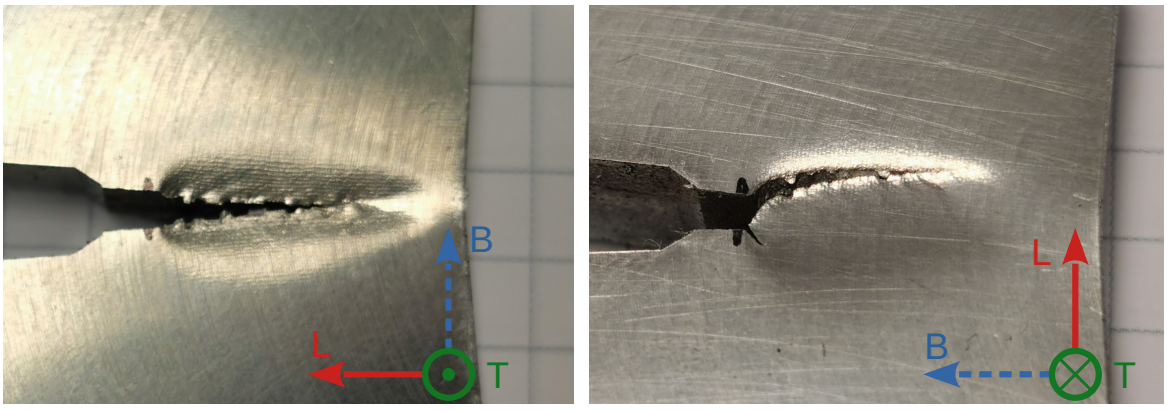

Figure 4: Macroscopic aspect of the cracks obtained during the fracture tests. Left : // specimen, Right : ⊥ specimen.

4. Discussion

The cracked specimens have been further studied in order to discuss the relationship between the fracture toughness anisotropy and the material's specific structure. First the material structure is analyzed in order to highlight the multi-scale character inherited from the building process (§4.1). Second, a fractographic analysis is performed to reveal the topology differences of the fracture surfaces with regard to the deposition strategy (§4.2). Finally, the fracture surface is correlated to the material structure to show at which scale the crack path is selected and to draw some explanations on the fracture toughness anisotropy (§4.3).

4.1. Material structure analysis

4.1.1. Additional sample preparation

The specimen labeled as 2// in section 3 was arbitrarily selected to perform an estimation of the ferrite and austenite contents, as well as to observe the material's meso- and micro-structures. Four cubic specimens (approximately 5 mm * 7 mm * 10 mm) were cut post-mortem in the bulk of the specimen. These were extracted in a region showing no macroscopic signs of plasticity, a few millimeters away from the crack surface. They were then tested through a SETARAM sigmameter to evaluate the rate of ferrite in the elaborated material. The measures are presented in §4.1.2.

Two of the cubes were then hot mounted, ground and polished following classical procedures, up to 1 µm diamond suspension. Different orientations were chosen for the two of them allowing to observe the plane perpendicular to the tracks (B-T) on one hand, and the plane parallel to the deposited layers (L-T) on the other. Note that these two plane orientations correspond to those of the machined notches for the ⊥ and // specimens respectively. Additionally, active oxide polishing has been performed using colloidal silica suspension (OP-S). The two orientation were then imaged by optical and scanning electron microscopy (SEM) with an Olympus Provis AX70 optical microscope and a ZEISS Evo10 SEM with filament respectively. The specimens were then electrolytically etched with a solution of 10% oxalic acid to further reveal the microstructure, which was observed by optical microscopy. The metallographic analysis stemming from these observations is presented in §4.1.3.

4.1.2. Ferrite content estimation

Due to the highly oriented nature of the material, each cubic sample was tested with the sigmameter in the 3 possible orientations. The ferrite phase is ferromagnetic contrarily to the austenite. Thus, the measure of the specific saturation magnetization of the material allows to estimate the ferrite proportion. The latter was computed using in-house EDF R&D knowledge, for which the domain of validity has not been fully verified on super DSS. Nevertheless the order of magnitude of the result is coherent with the optical analysis. Overall, the results do not depend on the orientation of the measure and are similar for the four samples, indicating that the distribution of the phases is homogeneous at the scale of the samples. The twelve measures give an average value of 76.8% of ferrite, with a standard deviation of 0.3.

4.1.3. Multi-scale metallographic analysis

The preparations made on the two considered orientations (L-T and B-T) allow to discuss the material structure on three scales of observation. First comes the mesoscale, where the structure directly depends on the deposition strategy. Second is the scale of a single track, in which HAZ are observed. The third and finest scale of interest corresponds to that of the metallic phases.

Mesostructure First, the whole mesostructure of the material is well revealed through the oxalic acid electrolytic etching (Figure 5). The material appears to be dense with low porosity on the considered polished planes. In a conservative approach, the micrograph of the region presenting the largest amount of porosities was selected (approximately 2000 x 1500 μm^2). It was thresholded using the imageJ software [35], leading to a density of 99.7 % estimated by pixel count. The other micrographs presented fewer pores, and this value is thought to be a lower bound for the average density in the elaborated material. Each individual track appears distinctly along both directions of observation. In the orthogonal plane (B-T), the structure of the tracks is fairly regular with a fish-scale like pattern (Figure 5, bottom). This shape, as well as the global structure, are highly dependent on the process parameters chosen for the deposition strategy. The characteristic dimensions of the laser scanning path, as well as the thermal history induced all come into play.

Single track scale : Heat-affected zones The second scale of observation corresponds to a single track. At this scale the thermal history has a particular effect on the microstructure. The deposition of subsequent tracks next to or on top of existing ones leads to the formation of heat-affected regions. These regions can be distinguished by the presence of small grains, as compared to the larger grains present in the heart of the tracks (primary solidification). This difference can be observed in both orientations (Figure 6). In addition to the grain boundaries, the oxalic acid electrolytic etching appears to have coloured the interior sections of the tracks, which have not been heat affected. The fish-scale shape observed in the (B-T) plane (Figure 6, right) is thought to be inherited from the melt pools. The semi-circular part therefore corresponds to the bottom of the deposited track, which reheats the neighbouring track previously deposited as well as the one in the layer underneath, forming HAZ in each of those. Then, the side and the top part of the considered track may themselves be reheated later, while the interior of the track is less affected. Hence, the interlayers are located at the semi-circular limit between the interior of the track and the HAZ. In the plane of the deposited layers (L-T), large elongated grains are oriented according to the direction of the deposition (Figure 6, left). The transverse cut also reveals large oriented grains in the interior region of the tracks (Figure 6, right). Therefore, these elongated grains form a complex columnar structure, which is inherited from the deposition strategy.

Phase distribution at the metallic grain scale Lastly, the third scale of interest to analyze corresponds to the metallic phases which could be directly observed by SEM after the OP-S polishing (Figure 7). Only the results obtained on the transverse orientation (B-T) are presented, as similar observations were made in the other orientation studied. The interior of the track and the heat-affected regions which have been distinguished at the upper scale show different phase distributions. The first region consists of large ferrite grains, which are separated by intergranular austenite. Emerging Widmanstätten austenite formations as described by Iams et al. [17] can also be seen. In the HAZ, the ferrite grains are smaller and a larger amount of intergranular austenite is observed. Additionally, numerous nodules of intragranular austenite have formed inside the ferrite grains.

Overall, the interior parts of the tracks are essentially ferritic regions, whereas the HAZ contains a larger proportion of austenite. This observation has to be confronted to the results of the sigmameter measures, which are presented in §4.1.2. The estimated value of 77% of ferrite appears congruent with the microstructure observations, since the austenite phase is nearly absent from the interiors of the tracks. Additionally, only small nodules have started to form in the HAZ for the intragranular form. The studied material is therefore largely ferritic, and notably far from the equilibrium proportions expected for this composition (Table 1), which should be closer to 50% of each phase.

In conclusion, the fabricated material's micro- and meso-structures are highly textured, following the strategy of deposition. Additionally, it appears to be relatively dense and no additional defects are observed. Three scales of interest appear from these observations, which raises the following question: which structural length and scale pilot the crack propagation ?

4.2. Fractography

Opening the specimens allowed the observation of the entire crack surfaces. Those were first studied on the macroscopic scale, then one specimen for each orientation (1// and 3⊥) was imaged by SEM.

4.2.1. Macroscopic observations

The two types of specimens show significantly different crack behaviors. The two types are illustrated in Figure 8, with the // (resp. ⊥) specimen on the left (resp. right). These crack behaviors are found to be repeatable, as the two specimens tested for each orientation were remarkably similar. It can be noted that for both orientations, the fatigue precrack is well aligned with machined notch, forming a particularly flat area compared to the rest of the crack surface.

For the // specimen, the crack broadly propagates in the symmetry plane of the sample. The crack surface is aligned with the initial machined notch as well as the fatigue precrack. However, jointly with the observations made on the side of the specimen (Figure 4), the surface is not perfectly flat and some grooves and track shapes are observed. For the ⊥ specimen, a complex tridimensional crack surface is observed. At the heart of the specimen the crack propagated straight, whereas near the surfaces the crack diverged from the symmetry plane, forming shear lips. These lips explain the deviation from straight crack growth observed on the side of the specimen (Figure 4). This fracture phenomenon is characteristic of finite thickness effects in some metallic materials [37, 32]. The terms of “slant" and “square" fracture for the shear lips on one hand and the straight propagation on the other are respectively used from here on. Slant fracture occurs in the regions in a state of plane stress, while the square fracture takes place in the middle of the specimen where plane strain dominates. The slant to square ratio measured is approximately 50%. Therefore, the slant fracture area is non negligible and thus the K_Q value estimated in section 3 is likely thickness dependent for the considered orientation.

Zuidema et al. [42] suggested that slant fracture is possible in materials presenting face-centered cubic structures (which is the case of austenite) or body-centered cubic structures (which is the case of ferrite) due to their numerous possible slip systems. Hence, there is likely a slip possibility near the direction of the maximum shear stress direction which allows the formation of the shear lips. Additionally, they state that the latter will always form unless there is a hindrance of the necessary slip in the 45° direction. This raises the question of their absence in the // specimens, which present a fully square fracture. Indeed, the thickness being the same for the two types of specimen, and the apparent rigidity being similar in both directions -as observed during the fracture tests (Figure 3)-, the areas in a state of plane stress or plane strain within the specimen should be identical in the two cases. It is thought that in the present case some weaknesses in the material structure may prevent the formation of the shear lips by favoring mode I failure in this orientation.

4.2.2. Microscopic observations

SEM observations of the crack surfaces offer a complimentary vision to the macroscopic observations, and are presented in Figure 9, at a 20x magnification. First, the // specimen is to be separated in different plateaus of various heights. Each of these plateaus appears to be locally flat. In comparison the ⊥ specimen, observed in the square section, appears more chaotic locally. These results contrast with the macroscopic observations, for which the // specimen showed the more tortuous crack surface, but at a smaller scale it is actually an assembly of flat sections. Altogether, the fracture mechanisms in both directions of interest are completely different at the two scales of observation which have been discussed, and an explanation for this is investigated in §4.3.

The SEM analysis of the specimens is completed by observations at smaller scales. A selection of images showing the characteristic features of the crack surfaces is presented in Figure 10. The reader is encouraged to find the complete SEM exploration in the online supplemental material, where the position of images with larger zoom levels are indicated on the lower magnification images, which allows to pinpoint the location of each feature. First, the images at a 100X magnification are considered (Figure 10, a and d). At this scale, the crack surfaces differ by their flatness as discussed earlier. However, they present similar features : a large number of spherical objects appear to be trapped in the surrounding material matrix. These objects are present all along the crack surfaces with characteristic sizes ranging between a few dozens of microns and 100 microns, which matches the sizes of the feedstock powder particles. Further examination of these object confirms that these objects are unmelted or semi-melted powder particles. Figure 10.b illustrates a characteristic spherical defect, which presents a satellite, on the surface of the // specimen. This particle appears to be cohesive with the matrix on the top side of the image. Figure 10.e shows the equivalent for the ⊥ specimen. This example seems partially melted on its bottom half and well fused with the rest of the material. Additionally, some pullout areas are also observed on the surfaces, as illustrated on the left side of Figure 10.c. These areas appear very smooth with some pullout marks or microcracks in the middle. They are thought to be the complimentary of a semi-melted particle present on the crack surface of the opposing half of the sample. Apart from these defects, the rest of the crack surface is entirely constituted of dimples (Figure 10, c and f). Those suggest that the crack essentially grows by microvoid coalescence. For both the // and ⊥ specimens, the dimples are well observed along the whole crack surfaces

apart from the semi-melted particles and the pullout areas. The dimples present similar sizes in the two specimens, which is of the order of the micron.

4.3. Material structure and fracture anisotropy

4.3.1. Qualitative observations

The fracture test results reported in section 3 show that the studied DSS presents a considerable anisotropy of fracture toughness, while the apparent stiffness is identical in the two tested directions. In §4.1.3, the particular structure of the studied material has been observed, which exhibits several length scales of interest : the well-defined scale of the mesostructure inherited by the deposition strategy, and the scales defined by the sizes of the grains, ranging from several dozens of microns for the large ferrite grains found in the interior of the tracks, to a few microns for the nodules of austenite found within the HAZ. Observation of the crack surfaces in §4.2 further highlights the differences in fracture mechanisms for both orientations, but does not provide definite answers to the question of the dominating length scale for fracture.

In order to determine which structural length scale pilots the fracture, the crack path within the material structure has been assessed. To do so, additional samples have been cut from the cracked CT specimens, in the (B-T) orientation for the // specimen and in the (L-T) orientation for the $\perp$ specimen. Considering Figure 8, the cut was performed across the area labeled “crack surface", at an approximate distance of 1 mm from the region labeled “fatigue precrack". The section obtained with this cut was submitted to the preparation protocol described in §4.1.1 to reveal the metallographic structure close to the crack surface.

An image of the structure near the crack surface for the // specimen is presented in Figure 11, left. The fracture surface is highlighted in red for visual clarity. It appears that this surface is preferentially tangent to the semi-circular shapes of the primary solidified melt pools revealed by the etching. As argued in §4.1.3, this limit between the HAZ and the semi-circular part of the interior of the track corresponds to the interlayer. Therefore, the interlayers are shown to be weaker than the core of the nearly fully ferritic region and constitute planes of weakness for crack propagation. The crack surface shown in Figure 11 presents some asperities. Those are formed by the crack when it selects different layers as it propagates. One can notice that these changes of layers of the crack surface often occur in the ferritic region, shown by some incomplete fish-scale patterns along the fracture surface. In horizontal direction however, no track is split in half by the crack surface, and the crack propagated only along the weak interlayer. This observation answers to the question of the dominant material scale length with regard to fracture : it is controlled by the mesostructure inherited by the fabrication strategy.

For the $\perp$ specimen, the structure near the crack surface is presented in Figure 11, right. The presented micrograph was taken in the square section of the crack surface. In that case, the crack surface was orthogonal to the deposited tracks, and the crack seems to propagate erratically across these. The resulting roughness may be caused by the presence of local defects randomly present in each track. In this orientation, the weak interlayers are not aligned with the crack and have to be crossed successively. In the slant section, which is not presented here, the observations were similar apart from the angle between the crack plane and the deposited tracks.

4.3.2. Roughness analysis

To support these observations, the roughness of the fracture surfaces was analyzed on images similar to those presented in Figure 11. Details about the procedure are given in Appendix A. The key elements are summarized in the present paragraph.

The 1D profile $h(z)$ formed by the crack surface (red lines in Figure 11) was extracted numerically over the whole specimen width for both orientations, and was analyzed in two ways. First, the scaling properties of the profiles were derived by studying the height-height correlation function [6, 31]:

$$\Delta h(\Delta z) = \langle \delta h(z, \Delta z)^2 \rangle_z^{1/2} \tag{3}$$

with

$$\delta h(z, \Delta z) = h(z + \Delta z) - h(z) \tag{4}$$

where Δz is a given distance between two points along the observed crack profile, h and z being the respective height and position along the profile of a given point (see Figure 11). This function is plotted in a logarithmic scale in Figure

12. By making the assumption of self-affine behavior up to a cutoff length ξ, the experimental data is fitted with a power law of the form [31] :

$$\frac{\Delta h}{l} = \left(\frac{\Delta z}{l}\right)^{\zeta} \tag{5}$$

which introduces the roughness exponent ζ and the topothesy length l. These three parameters were found to have similar values for both orientations within experimental precision, with $l \approx 40$ µm, $\xi \approx 550$ µm, and ζ between 0.7 and 0.8. Thus, a classic roughness analysis does not allow to discriminate the two orientations, at least from the 1D data collected on the two studied specimens. Note that the roughness exponent values found are characteristic of ductile failure according to the literature [5, 30], in agreement with the observation of dimples at the microscale in §4.2.2.

A second method was considered to correlate the extracted profiles with the material's structure, in accordance with the qualitative observations presented in Figure 11. While the computation of the height-height correlation function yields a single scalar value for a given spacing Δz (Equation 3), the whole distribution of $\delta h(z, \Delta z)$ values obtained when z scans the whole profile width (Equation 4) can be studied for well chosen values of Δz. The second analysis consists in the examination of such distributions when Δz is equal to a characteristic length of the material structure. The mean dimensions of the tracks were measured from the micrographs of the etched material, giving average values of $H_m = 203$ µm for the height and $W_m = 374$ µm for the width. The distributions of the $\delta h(z, \Delta z)$ values obtained for $|\Delta z| = W_m$ are studied in the following. The motivation to do so is that for this choice of length, this procedure is physically equivalent to look at the changes in height between each neighbouring tracks. If there is no specific feature guiding the crack, then the distribution of $\delta h(z, \Delta z)$ values is expected to be centered around 0, with a certain amount of dispersion which is assumed to be random. However, if the assumption of the interlayers being weak planes for propagation is correct, δh should be close to 0 if for two neighbouring tracks the crack propagates within the same relatively flat interlayer. However, if the crack jumps from a weak interlayer to the next one, as is assumed in Figure 11, then $|\delta h|$ should be approximately equal to the thickness of a layer, which is also the height of a single track $H_m \approx 200$ µm. In the same way, if the crack jumps between n consecutive interlayers, $|\delta h|$ should be close to $n * H_m$ within a certain dispersion.

The probability densities associated with the $\delta h(z, \Delta z)$ distributions obtained for $|\Delta z| = W_m$ are represented for both orientations as histograms in Figure 13. Both densities could be reasonably well fitted with a Gaussian mixture model (GMM) [3, 19]. The // orientation was fitted with a five-component GMM (Figure 13, left). Each of the Gaussian components was found the be centered around a multiple of 200 µm. This is in agreement with the interlayers being weak planes for fracture, as explained previously. In particular, the peaks centered around $\pm$ 400 µm are interpreted as a jump of two layers simultaneously, within the spawn of a track's width. On the other hand, for the $\perp$ orientation the distribution was well approached by a single Gaussian curve centered around $\delta h = 0$ (Figure 13, right), which is in agreement with a straight propagation presenting no specific planes of weakness and random variations in height. In summary, analyzing the changes in height of the crack surface profiles, with the track width W_m as sole *a priori* knowledge, allowed to retrieve the track height H_m from the // orientation data, while a simple random model was found to approach the $\perp$ values reasonably well.

To ensure that the mesostructure is indeed the scale which dominates the fracture, the same analysis has been performed for other orders of magnitude of Δz. The probability densities obtained for $|\Delta z| = W_m/10$ and for $|\Delta z| = W_m/100$ are represented in Figure 14 and Figure 15 respectfully. Relatively to the observed microstructure (see Figure 7), these orders of magnitudes respectively approach the size of the ferrite grains in the interior of the tracks on one hand, and the size of the intragranular austenite nodules on the other. In each case, the distributions were found to follow the normal law as in the $\perp$ case for $|\Delta z| = W_m$. Therefore, no characteristic length of the height variations could be found at scales different than the mesostructure.

4.3.3. Fracture mechanisms

These conclusions provide an explanation for the observed differences in fracture mechanisms for the two tested orientations. For the $\perp$ specimens, the crack has to propagate across the layers and tracks. These do not contain systematic weaknesses oriented in the propagation direction, and the crack surface may be defined by some local inhomogeneities within each track. The final surface may therefore be rough due to the randomness of local weaknesses. Additionally, the absence of a particular weakness in the direction of crack growth allows the material to form the shear lips described in §4.2.1. For the // specimens on the other hand, the crack is aligned with the weak interlayers, which facilitates its growth. The obtained crack surface are thus locally flat, following the deposition strategy. Additionally,

these weak planes may facilitate propagation to the point that it occurs before that the shear in the 45° direction gets sufficiently large, and the associated slip cannot occur. Thus, the macroscopic shear lips cannot be formed and the global crack surface is of the square type. The track and grooves that can be observed at the macroscopic scale (See Figure 8) are explained by the aforementioned changes of interlayer as the crack propagates. A possible explanation for these changes of interlayer would be the presence of local weaknesses caused by local defects. For instance, the local density of the unmelted or semi-melted particles may be in cause, assuming that they are weaknesses. This would explain the large number of particles observed with the SEM, as the crack front would select its path among the few middlemost interlayers.

5. Conclusion

In this study, the fracture behavior of a duplex stainless steel manufactured by directed energy deposition has been investigated. Dense volumes have been fabricated, allowing to manufacture compact tensile specimens in different orientations with regard to the main directions of the deposition strategy. The two orientations chosen were either with an initial notch machined parallel to the tracks and layers, or with the notch perpendicular to those. Fracture tests were performed to evaluate fracture properties of the material. The apparent stiffness is found to be the same for the two tested orientations, but a marked anisotropy of fracture is observed : both the fracture toughness values and the macroscopic aspects of the crack propagation are found different. Additional discussions, stemming from the multiscale analysis of the material structure and from fractography, propose an explanation for this anisotropy :

- Several scales of interest of the structure are exhibited : the mesoscale inherited by the deposition strategy (several hundreds of microns), and the finer scales defined by the grain sizes, depending on the area considered (ranging from a few microns to several dozens of microns).
- The examination of sections cut orthogonally to the crack surfaces reveals that the interlayers constitute planes of weakness for crack propagation. Therefore, the scale mainly responsible for the fracture anisotropy is defined by the mesostructure. This provides explanations for all the differences which were observed on the crack surfaces at the macroscopic and the microscopic scales.

Acknowledgements

The work was partially supported by Agence de l'Innovation de Défense – AID - via Centre Interdisciplinaire d'Etudes pour la Défense et la Sécurité – CIEDS - (projects 2018 - PoroCrack, 2020 - QUADS and 2022 - FracAddi).

The authors wish to thank the QUADS project for providing the DSS powder. Our thanks go in particular to Fabien Szmytka and Sebastien Ballesio, as well as Baris Telmen, who provided us with the processing parameters in addition to helpful discussions. We also thank Emeric Brantus from EDF for performing the sigmameter measures, Lahcène Cherfa and Matthieu Roy for specimen machining, Pierre-Louis Hanappier for his support on the BeAM *Mobile* machine, as well as Nicolas Thurieau for his help with the experiments. We also thank Daniel Bonamy for his help on the study of the fracture surface roughness.

Data availability

Data will be made available on request.

A. Details of the roughness analysis

In order to support the qualitative observations made on Figure 11 and the resultant discussion, a roughness analysis has been performed on the observed crack surface profiles over the entire thickness of the specimens.

Face observed	W_m (µm)	H_m (µm)
// - NP	378 ± 5	206 ± 1
// - OP	381 ± 5	200 ± 1
⊥ - NP	373 ± 5	N/A
⊥ - OP	365 ± 5	N/A

Table 3
Mean values of the track dimensions measured on the images of the etched faces. W_m : mean width, H_m : mean height.

A.1. Extraction of the crack surface profiles

As described in §4.3.1, one specimen for each direction was selected to perform an orthogonal cut with regard to the crack surfaces, providing the images presented in Figure 11. This figure only presents one section for each specimen, but two opposing faces were obtained from the cut, separated by a distance equal to the thickness of the cutting saw i.e. approximately 1 mm. All four faces were prepared as described in §4.1.1, including etching. Therefore, for each orientation, two sections can be observed. The first one, which is at an approximate distance of 1 mm from the final precrack front, will be labeled “NP" (next to precrack). The second one, is the opposite face and therefore distant of approximately 2 mm from the final precrack front will be labeled “OP" (opposite to precrack). For each face, optical microscope images were taken along the whole thickness of the specimen, at 100x magnification. The considering pixel size was measured to be equal to 0.7 µm approximately. Then, the whole crack surface was reconstructed by automated image stitching. From these images, the width of a dozen of tracks was manually measured for each orientation to estimate the average track width W_m, which are reported in Table 3. Additionally, it was also possible to measure the track heights H_m on the specimen in the // orientation. These values can be compared to the printing strategy presented in §2.1. The measured heights are in very good agreement, while there is a small difference for the widths which were expected to be equal to 390 µm.

The available pictures were found to be insufficient to obtain the profile of the crack surface over the whole specimen thickness, because of the etching step which made some of the colored areas indistinguishable from the mounting resin on the images due to insufficient contrast. Hence, the specimens were carefully re-polished up to the 1 µm diamond suspension step, providing mirror finish surfaces. While the information of the material structure was lost by doing so, the re-polished surface provided excellent contrast with the mounting resin which allowed to detect the profile formed by the crack surfaces over the thickness of the specimens. The surfaces corresponding to the shear lips in the ⊥ specimen were removed from the study as they present a 45° angle with the horizontal direction. A similar length was also removed on each side of the // specimen images for coherence. From here on, such a crack surface observed horizontally is considered with the following axis system : the z axis refers to the position along the thickness of the specimen, and h designs the height of the surface at a given z value. Automatic edge detection was performed with a Python script. First, the image is binarized using Otsu’s Method [26, 40]. The resulting image was cleaned up from small defects by performing a binary hole filling operation and a binary opening operation (3 iterations, disk structure element). Then, the edge detection was performed by using the Canny algorithm [9, 40]. The resulting line obtained cannot be considered as a profile to study yet because for a few values of z, multiple points of different heights belong the the detected edges. The conversion to a profile of the form $h = f(z)$ is done by selecting, for each z value, the point with the maximum height encountered. One profile for each orientation is illustrated in Figure 16.

A.2. Scaling properties analysis

The roughness of each profile was analyzed following the methods presented by Bouchaud et al. [6], Ponson et al. [31], under the hypothesis that they present self-affine behaviors. First, the height-height correlation function, defined by Equation 3 is calculated. It is illustrated in logarithmic scales in Figure 12 for the face // - NP. The linear portion in the logarithmic representation is fitted with a power-law (Equation 5). introducing the parameters ζ which is the roughness exponent, and l the topothesy length. The additional parameters considered are the maximum Δh value, and the cutoff length ξ, which are both indicated in Figure 12 (face // - NP) with the horizontal and vertical dotted lines respectfully.

The values obtained for these parameters for each face are indicated in Table 4. All roughness exponents were found to be comprised between 0.7 and 0.8. Both NP profiles presented lower values than their counterparts, but the low number of profiles analyzed does not allow to confirm if this is a tendency or only an effect of experimental dispersion. The topothesy lengths show no tendency at all, neither do the values of Δh_{max}. Finally, the cutoff values ξ

Face	ζ	l (µm)	ξ (µm)	Δh_{max} (µm)
// - NP	0.73	43	530	271
⊥ - NP	0.71	59	585	301
// - OP	0.80	35	521	300
⊥ - OP	0.78	26	704*	340*

Table 4
Roughness parameters obtained for each face observed : Roughness exponent ζ, Topothesy length l, Cutoff length ξ, maximum value of Δh. The * symbol indicates uncertain results (see text).

appear to be larger for the ⊥ specimen, but once again it may be within experimental dispersion. In particular, these values are especially sensitive to the fit of the power law considered. It has to be noted that contrarily to the other faces, the height-height correlation function obtained for the face ⊥ - OP presented it's maximum value Δh_{max} at the largest value of Δz considered (half the total width of the profile) making this value and the associated cutoff ξ uncertain. Most importantly, none of the estimated lengths seem to relate to the characteristic dimensions of the tracks presented in Table 3.

A.3. Whole δh distributions for $\Delta z = W_m$

According to Equation 3, for a given length Δz, the root mean square of the corresponding height variations $\delta h(z, \Delta z)$ is calculated. In the following, the whole distribution of values is examined, for a well chosen length $\Delta z = W_m$. In order to analyze the largest possible sets of values, the $\delta h(z, \Delta z)$ values obtained from both analyzed faces are merged into a single large set for each orientation. From a physical point of view, the sign of the height difference changes whether the profile is examined from the left to the right or the opposite, *i.e.* whether Δz is positive or negative. This, in combination with the limited amount of data available, leads to asymmetric distributions of $\delta h(z, \Delta z)$ for $\Delta z = W_m$, as represented in figure 17 in blue. In this figure, the probability densities of both distributions are represented on histograms plotted on 50 bins in the [-500 µm, +500 µm] range. Thus, each bin has a width of 20 microns. In order to avoid the bias of the sign of Δz, one solution could be to consider the set of absolute values $|\delta h|$ instead. However this solution would provide a folded distribution which will be an inconvenience for the model proposed in the following. Instead, another solution was chosen in the present work, consisting to study the superset built by merging the values for $\Delta z = W_m$ and those for $\Delta z = -W_m$:

$$\{\delta h\}_{|\Delta z|=W_m} = \{\delta h\}_{\Delta z=W_m} \cup \{\delta h\}_{\Delta z=-W_m} \tag{6}$$

This has for effect to double the total number of values in the sets, but has no effect on the analysis since the following considerations are made on the associated probability densities. The latter are represented in Figure 17 in orange. The obtained histograms are symmetrized versions of the previous ones, which evacuates the bias of the sign of Δz. Note that studying the superset is nearly equivalent to studying the set of values of $|\delta h|$ previously evoked. Indeed, restricting the graphs in Figure 17 to the positive values of δh only yields exactly the same histogram that would have been obtained with the set of $|\delta h|$ values. Therefore, both of these contain the same information, but studying the superset allows to avoid having to deal with folded normal distributions.

A.4. Modeling of the probability densities

While the histogram obtained for the ⊥ specimen seems to be reasonably well approached by a single Gaussian distribution (Figure 13, right), multiple peaks can be observed for the // specimen. A Gaussian mixture model (GMM) is proposed to fit this distribution [3, 19]. Mixture models make the assumption that the fitted distribution can be divided into K sub-populations [39]. In particular, GMMs make the choice of representing each sub-population with a normal distribution described by its mean value μ, its standard deviation σ and its relative weight within the whole population. The optimisation of the model can be done classically by using the expectation–maximization (EM) algorithm [14]. In this work, the implementation found in the Scikit-learn Python package [29] was used. It was found that the data was well approached with a five-component model (Figure 13, left), and the characteristics of each Gaussian component are indicated in Table 5. The characteristics of the single Gaussian used to fit the ⊥ case are also indicated in the table. Note that by nature the EM algorithm converges towards a local maximum therefore several optimisation results can be obtained. In particular, non symmetrical mixtures can be obtained, which is not physically acceptable. Due to this, an initial guess with the vector [0, 200, -200, 400, -400] (in µm) for the means was introduced in the algorithm, based on observation of the histogram in Figure 17.

Orientation	Component	Mean μ (µm)	Std. dev. σ (µm)	Weight (%)
//	1	0	60	56
	2	197	48	19
	3	-197	48	19
	4	390	49	3
	5	-390	48	3
⊥	1	0	144	100

Table 5
Parameters of the Gaussian components used to fit the probability densities of the $\delta h(W_m)$ values for both orientations, for $\Delta z = W_m$.

The case of the ⊥ specimen is the simplest to discuss : fitting the distribution of the $\delta h(z, \Delta z)$ values with a normal distribution is coherent with the theory of a random formation of the crack surface. The mean value of 0 µm suggests that the horizontal plane is the expected plane for fracture, and the dispersion of the values comes from the random local departures from the expected direction. In the case of the // specimen, it appears that each Gaussian component is well centered around a multiple of the layer height, as measured in Table 3. Therefore, each component is associated with the probability of the crack to jump from one interlayer to another. Additionally, it is found that all the standard deviations of the components are of similar magnitude, which is smaller than that of the ⊥ case. This suggests that the crack growth is indeed favored and guided by the interlayers, as the random scatter around the expected values is smaller than that observed for the ⊥ specimen. Finally, the comparison of the Gaussian component weights confirms that the most likely outcome (56% chance) is that the crack remains on the same interlayer in the spawn of a single track width. This is in agreement with the flatness of the plateaus described in §4.2.2. Then, the presence of multiple plateaus are in accordance with the probability of the crack jumping between interlayers (38% chance for a jump of the height of a layer, and 6% chance for a jump of 2 layers). Note that these values for the weights are dependent on the specific profiles analyzed in a certain measure, but still validate the idea of the interlayers being planes of weakness for crack propagation.

To ensure the objectivity of the proposed models for each orientation, these have been swapped between the two datasets for comparison purposes. The distributions fitted with the swapped models are represented in Figure 18. For the // orientation, the single Gaussian fit does not accurately fit the data, especially considering the highest values predicted by the model. On the other hand, the five-component GMM fit offers a satisfying representation of the data from the ⊥ orientation. However, in this case the Gaussian components centered around $\delta h = 0$ and $\pm$ 150 µm aren't separated as clearly as for the // data (Figure 13), and the other two have negligible weights (≈1%). Even though this model cannot be directly rejected, it is unclear whether it is a better fit than the single Gaussian or not, and it may be overfitting the data. In all cases, the shape of the total mixture is not fundamentally different from the single Gaussian representation, and the latter should be preferred following Occam's razor principle.

A.5. Other orders of magnitude for Δz

The same analysis was performed for other orders of magnitude of Δz to verify if other characteristic lengths could also be extracted from those. The values chosen for Δz were $W_m/10 \approx 40$ µm, and $W_m/100 \approx 4$ µm. While in the case of $|\Delta z| = W_m$ the whole datasets could be used to fit a model, for the two other scales considered it was found that the sets included a small amount of values unusually large compared to the rest of the data. Those outliers were removed from the data by using the classic IQR method : the interquartile range (IQR) was calculted as $IQR = Q_3 - Q_1$ where Q_1 and Q_3 are the first and third quartiles respectfully. Then, any value larger than $Q_3 + 1.5 * IQR$ or smaller than $Q_1 - 1.5 * IQR$ was considered to be an outlier and removed from the data to fit. Then, the sets for both orientations could be fitted accurately with a single Gaussian curve, for both values of Δz. These are represented and compared to the corresponding histograms in Figures 14 and 15. Note that in the case of $|\Delta z| = W_m/100$, a maximum of 30 bins could be used for the histogram representation, as a larger number would make the bin width smaller than the pixel size of the images, which is not acceptable. Hence, apart from the // orientation with $|\Delta z| = W_m$, all distributions were found to follow a normal law centered around zero, and no characteristic length could be found.

References

[1] Balit, Y., Charkaluk, E., Constantinescu, A., 2020a. Digital image correlation for microstructural analysis of deformation pattern in additively manufactured 316L thin walls. Addit. Manuf. 31, 100862. doi:10.1016/j.addma.2019.100862.

[2] Balit, Y., Joly, L.R., Szmytka, F., Durbecq, S., Charkaluk, E., Constantinescu, A., 2020b. Self-heating behavior during cyclic loadings of 316L stainless steel specimens manufactured or repaired by Directed Energy Deposition. Mater. Sci. Eng.: A 786, 139476. doi:10.1016/j.msea.2020.139476.

[3] Banfield, J.D., Raftery, A.E., 1993. Model-Based Gaussian and Non-Gaussian Clustering. Biometrics 49, 803–821. doi:10.2307/2532201, arXiv:2532201.

[4] Becker, T.H., Kumar, P., Ramamurty, U., 2021. Fracture and fatigue in additively manufactured metals. Acta Mater. 219, 117240. doi:10.1016/j.actamat.2021.117240.

[5] Bonamy, D., Ponson, L., Prades, S., Bouchaud, E., Guillot, C., 2006. Scaling Exponents for Fracture Surfaces in Homogeneous Glass and Glassy Ceramics. Phys. Rev. Lett. 97, 135504. doi:10.1103/PhysRevLett.97.135504.

[6] Bouchaud, E., Lapasset, G., Planès, J., 1990. Fractal Dimension of Fractured Surfaces: A Universal Value? EPL 13, 73. doi:10.1209/0295-5075/13/1/013.

[7] Brázda, M., Salvetr, P., Dlouhý, J., Vavřík, J., 2020. Influence of laser power in direct laser deposition on the proportion of ferrite and austenite in duplex steel SAF2507, in: METAL 2020, pp. 539–544. doi:10.37904/metal.2020.3517.

[8] Cain, V., Thijs, L., Van Humbeeck, J., Van Hooreweder, B., Knutsen, R., 2015. Crack propagation and fracture toughness of Ti6Al4V alloy produced by selective laser melting. Addit. Manuf. 5, 68–76. doi:10.1016/j.addma.2014.12.006.

[9] Canny, J., 1986. A Computational Approach to Edge Detection. IEEE Trans. Pattern Anal. Mach. Intell. PAMI-8, 679–698. doi:10.1109/TPAMI.1986.4767851.

[10] Corre, T., Lazarus, V., 2021. Kinked crack paths in polycarbonate samples printed by fused deposition modelling using criss-cross patterns. Int. J. Fract. 230, 19–31. doi:10.1007/s10704-021-00518-x.

[11] Dass, A., Moridi, A., 2019. State of the Art in Directed Energy Deposition: From Additive Manufacturing to Materials Design. Coatings 9, 418. doi:10.3390/coatings9070418.

[12] DebRoy, T., Wei, H., Zuback, J., Mukherjee, T., Elmer, J., Milewski, J., Beese, A., Wilson-Heid, A., De, A., Zhang, W., 2018. Additive manufacturing of metallic components – Process, structure and properties. Prog. Mater. Sci. 92, 112–224. doi:10.1016/j.pmatsci.2017.10.001.

[13] Delahaye, J., Tchuindjang, J.T., Lecomte-Beckers, J., Rigo, O., Habraken, A.M., Mertens, A., 2019. Influence of Si precipitates on fracture mechanisms of AlSi10Mg parts processed by Selective Laser Melting. Acta Mater. 175, 160–170. doi:10.1016/j.actamat.2019.06.013.

[14] Dempster, A.P., Laird, N.M., Rubin, D.B., 1977. Maximum Likelihood from Incomplete Data Via the EM Algorithm. J. R. Stat. Soc. Series B Stat. Methodol. 39, 1–22. doi:10.1111/j.2517-6161.1977.tb01600.x.

[15] Gunn, R.N., 1998. Duplex Stainless Steels Microstructure, Properties and Applications. Anti-corros. Method. M. 45. doi:10.1108/acmm.1998.12845bae.001.

[16] Herzog, D., Seyda, V., Wycisk, E., Emmelmann, C., 2016. Additive manufacturing of metals. Acta Mater. 117, 371–392. doi:10.1016/j.actamat.2016.07.019.

[17] Iams, A.D., Keist, J.S., Palmer, T.A., 2020. Formation of Austenite in Additively Manufactured and Post-Processed Duplex Stainless Steel Alloys. Metall. Mater. Trans. A 51, 982–999. doi:10.1007/s11661-019-05562-w.

[18] ISO12135:2016, 2016. Metallic Materials — Unified Method of Test for the Determination of Quasistatic Fracture Toughness. Technical Report.

[19] Jain, A.K., Murty, M.N., Flynn, P.J., 1999. Data clustering: A review. ACM Comput. Surv. 31, 264–323. doi:10.1145/331499.331504.

[20] Khosravani, M.R., Berto, F., Ayatollahi, M.R., Reinicke, T., 2020. Fracture behavior of additively manufactured components: A review. Theor. Appl. Fract. Mech. 109, 102763. doi:10.1016/j.tafmec.2020.102763.

[21] Kumar, P., Prakash, O., Ramamurty, U., 2018. Micro-and meso-structures and their influence on mechanical properties of selectively laser melted Ti-6Al-4V. Acta Mater. 154, 246–260. doi:10.1016/j.actamat.2018.05.044.

[22] Kumar, P., Ramamurty, U., 2019. Microstructural optimization through heat treatment for enhancing the fracture toughness and fatigue crack growth resistance of selective laser melted Ti6Al4V alloy. Acta Mater. 169, 45–59. doi:10.1016/j.actamat.2019.03.003.

[23] Kumar, P., Zhu, Z., Nai, S.M.L., Narayan, R.L., Ramamurty, U., 2021. Fracture toughness of 304L austenitic stainless steel produced by laser powder bed fusion. Scr. Mater. 202, 114002. doi:10.1016/j.scriptamat.2021.114002.

[24] Ngo, T.D., Kashani, A., Imbalzano, G., Nguyen, K.T., Hui, D., 2018. Additive manufacturing (3D printing): A review of materials, methods, applications and challenges. Compos. B. Eng. 143, 172–196. doi:10.1016/j.compositesb.2018.02.012.

[25] Nilsson, J.O., 1992. Super duplex stainless steels. Mater. Sci. Technol. 8, 685–700. doi:10.1179/mst.1992.8.8.685.

[26] Otsu, N., 1979. A Threshold Selection Method from Gray-Level Histograms. IEEE Trans. Syst. Man Cybern. Syst. 9, 62–66. doi:10.1109/TSMC.1979.4310076.

[27] Paul, M.J., Liu, Q., Best, J.P., Li, X., Kruzic, J.J., Ramamurty, U., Gludovatz, B., 2021. Fracture resistance of AlSi10Mg fabricated by laser powder bed fusion. Acta Mater. 211, 116869. doi:10.1016/j.actamat.2021.116869.

[28] Paul, M.J., Muniandy, Y., Kruzic, J.J., Ramamurty, U., Gludovatz, B., 2022. Effect of heat treatment on the strength and fracture resistance of a laser powder bed fusion-processed 18Ni-300 maraging steel. Mater. Sci. Eng.: A 844, 143167. doi:10.1016/j.msea.2022.143167.

[29] Pedregosa, F., Varoquaux, G., Gramfort, A., Michel, V., Thirion, B., Grisel, O., Blondel, M., Prettenhofer, P., Weiss, R., Dubourg, V., Vanderplas, J., Passos, A., Cournapeau, D., Brucher, M., Perrot, M., Duchesnay, É., 2011. Scikit-learn: Machine Learning in Python. J. Mach. Learn. Res. 12, 2825–2830.

[30] Ponson, L., Auradou, H., Pessel, M., Lazarus, V., Hulin, J.P., 2007. Failure mechanisms and surface roughness statistics of fractured Fontainebleau sandstone. Phys. Rev. E 76, 036108. doi:10.1103/PhysRevE.76.036108.

[31] Ponson, L., Bonamy, D., Barbier, L., 2006. Cleaved surface of i-AlPdMn quasicrystals: Influence of the local temperature elevation at the crack tip on the fracture surface roughness. Phys. Rev. B 74, 184205. doi:10.1103/PhysRevB.74.184205.

[32] Pook, L.P., 2013. A 50-year retrospective review of three-dimensional effects at cracks and sharp notches. Fatigue Fract. Eng. Mater. Struct. 36, 699–723. doi:10.1111/ffe.12074.

[33] Quénard, O., Dorival, O., Guy, Ph., Votié, A., Brethome, K., 2018. Measurement of fracture toughness of metallic materials produced by additive manufacturing. CEAS Space J. 10, 343–353. doi:10.1007/s12567-018-0202-z.

[34] Sanaei, N., Fatemi, A., 2021. Defects in additive manufactured metals and their effect on fatigue performance: A state-of-the-art review. Prog. Mater. Sci. 117, 100724. doi:10.1016/j.pmatsci.2020.100724.

[35] Schneider, C.A., Rasband, W.S., Eliceiri, K.W., 2012. NIH Image to ImageJ: 25 years of image analysis. Nat. Methods 9, 671–675. doi:10.1038/nmeth.2089.

[36] Srawley, J.E., 1976. Wide range stress intensity factor expressions for ASTM E 399 standard fracture toughness specimens. Int. J. Fract. 12, 475–476. doi:10.1007/BF00032844.

[37] Srawley, J.E., Brown, W.F., 1965. Fracture Toughness Testing. Technical Report. National Aeronautics and Space Administration.

[38] Suryawanshi, J., Prashanth, K.G., Ramamurty, U., 2017. Mechanical behavior of selective laser melted 316L stainless steel. Mater. Sci. Eng.: A 696, 113–121. doi:10.1016/j.msea.2017.04.058.

[39] Titterington, D., Smith, A., Makov, U., 1985. Statistical Analysis of Finite Mixture Distributions. John Wiley & Sons Inc., New York.

[40] van der Walt, S., Schönberger, J.L., Nunez-Iglesias, J., Boulogne, F., Warner, J.D., Yager, N., Gouillart, E., Yu, T., 2014. Scikit-image: Image processing in Python. PeerJ 2, e453. doi:10.7717/peerj.453.

[41] Zhang, D., Liu, A., Yin, B., Wen, P., 2022. Additive manufacturing of duplex stainless steels - A critical review. J. Manuf. Process. 73, 496–517. doi:10.1016/j.jmapro.2021.11.036.

[42] Zuidema, J., Veer, F., Van Kranenburg, C., 2005. Shear lips on fatigue fracture surfaces of aluminum alloys. Fatigue Fract. Eng. Mater. Struct. 28, 159–167. doi:10.1111/j.1460-2695.2004.00837.x.

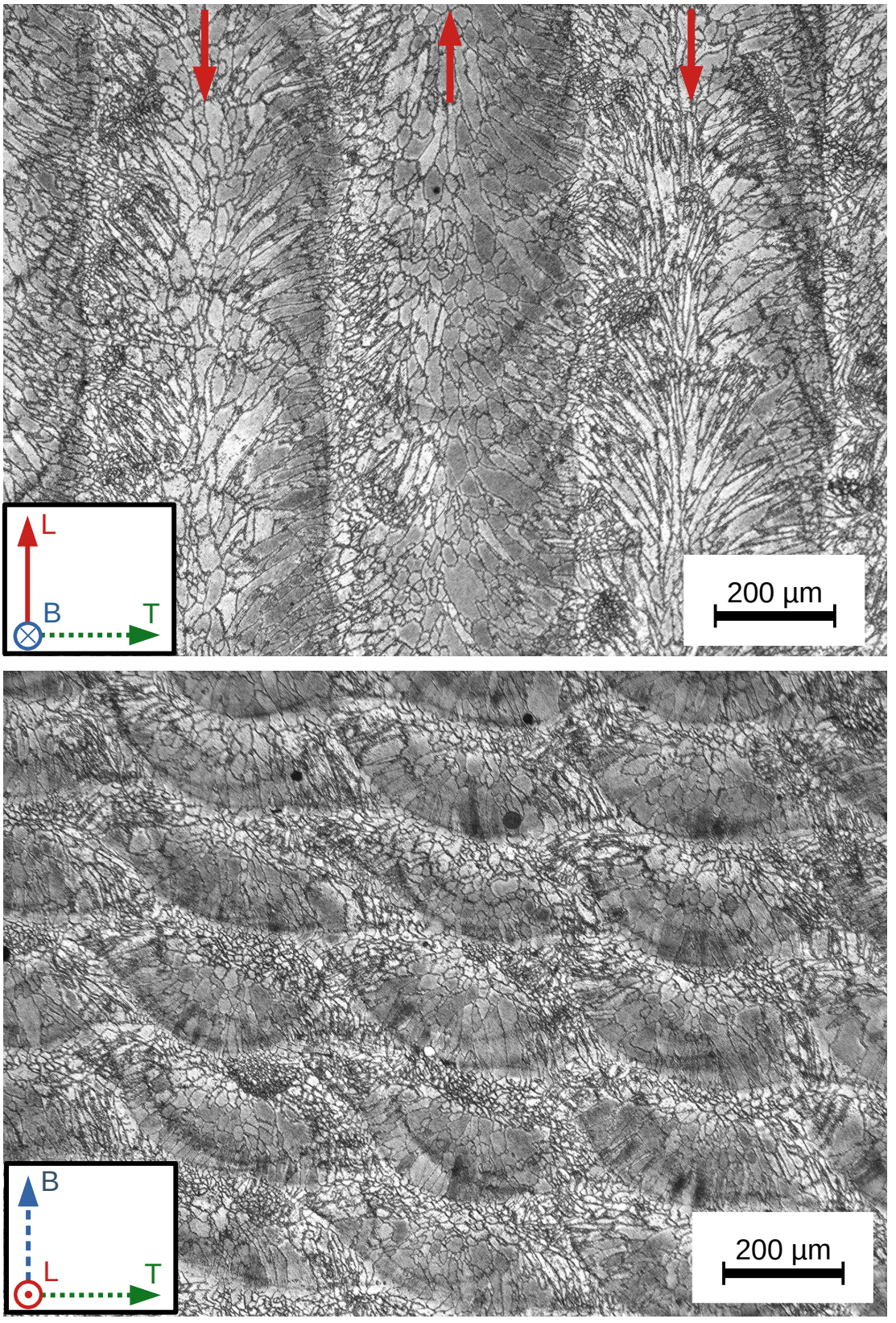

Figure 5: Optical microscope observation of the mesostructure revealed after electrolytic etching with 10% oxalic acid. Top : Plane of the layers. Red arrows indicate the direction of deposition for each track. Bottom : Plane perpendicular to the tracks.

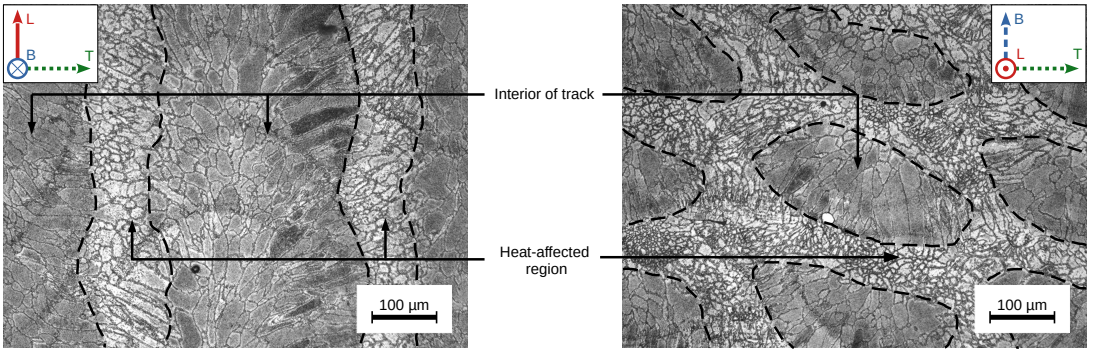

Figure 6: Optical microscope observation of both orientations at the scale of a few tracks, after electrolytic etching with 10% oxalic acid. Black hashed lines indicate the delimitation between the two types of regions. Left : Plane of the layers. Right : Plane perpendicular to the tracks.

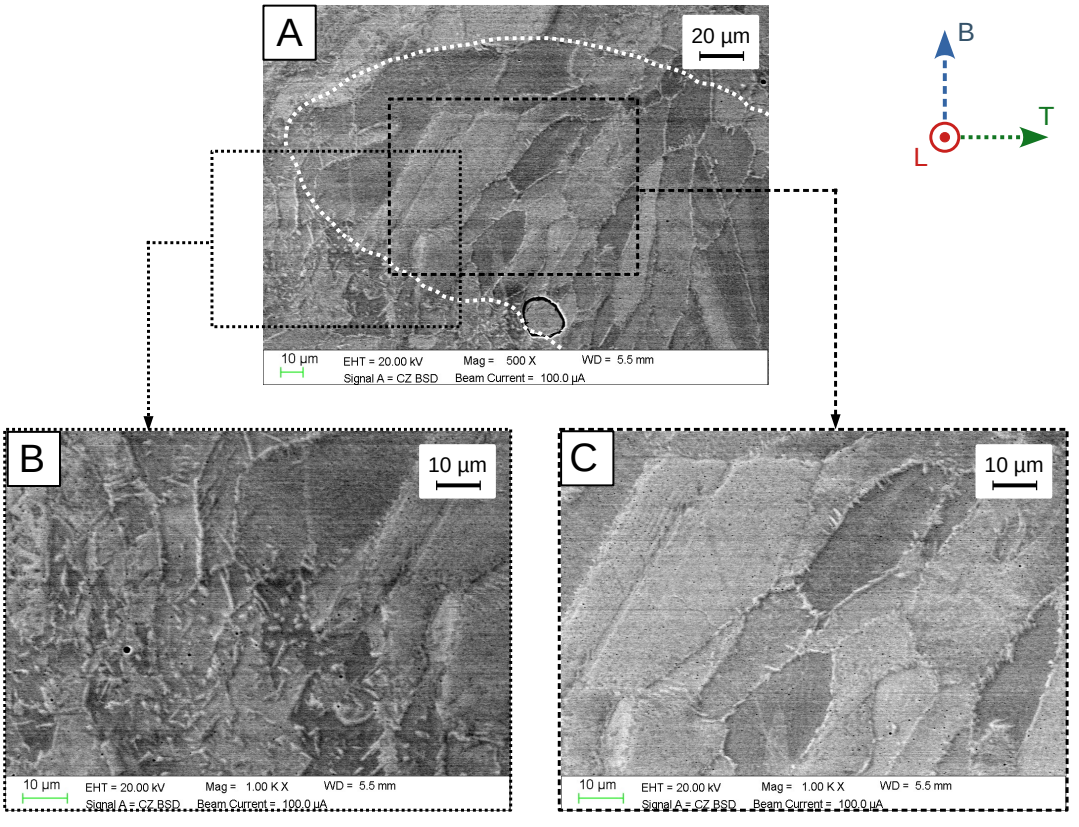

Figure 7: SEM observations of the different phases in the two regions described in Figure 6. A) Scale of a single track. The white dotted line represents the approximate frontier between the two regions. B) Nodules of intragranular austenite in the HAZ region. C) Large ferrite grains and intergranular austenite in the interior of the track.

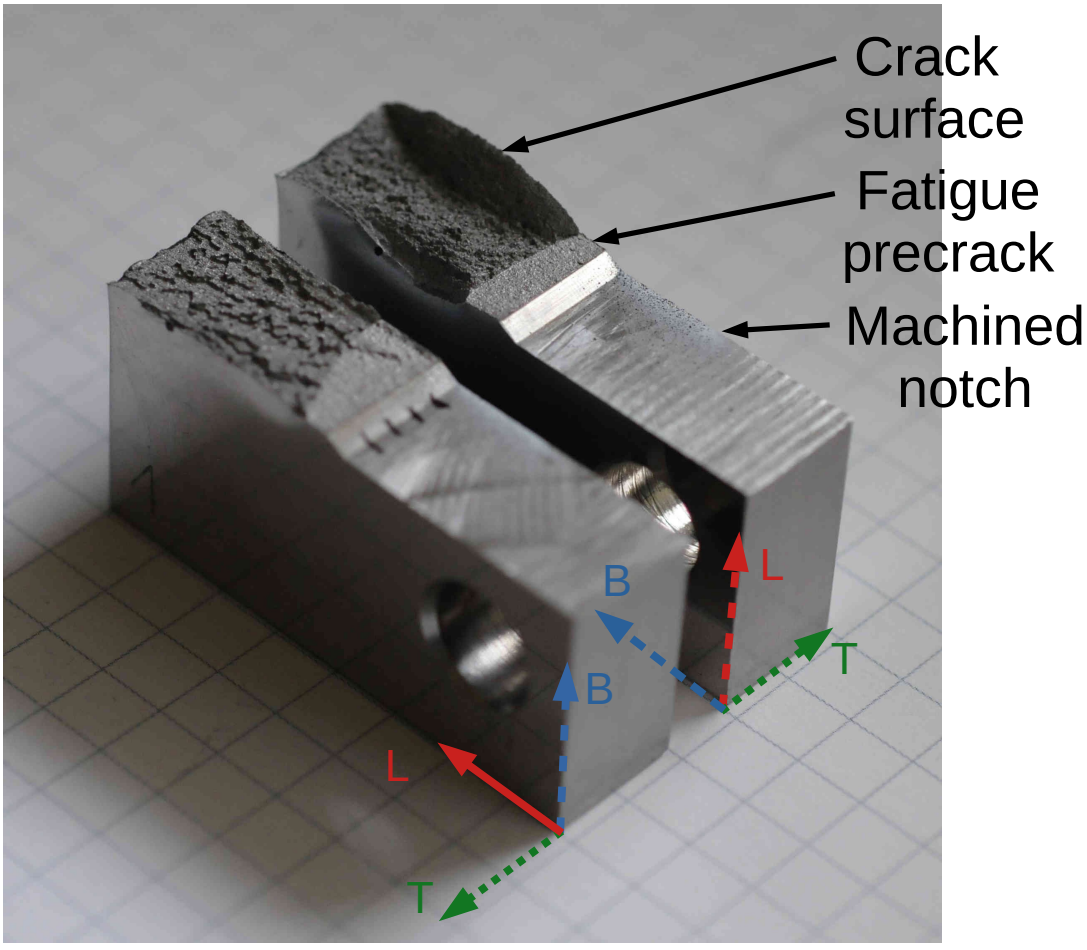

Figure 8: Macroscopic crack aspect of the crack surfaces obtained for each type of specimen. Left : // specimen. Right : ⊥ specimen.

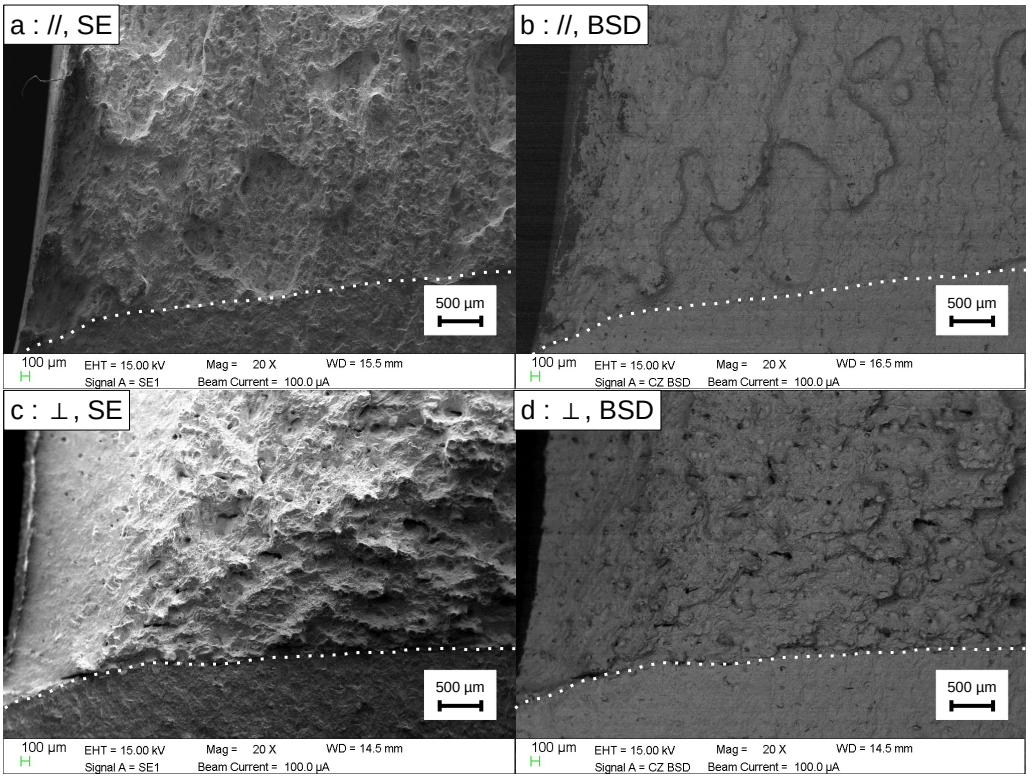

Figure 9: SEM observations of the crack surface near the fatigue precrack for a // specimen (a, b) and a ⊥ specimen (c, d). The views capture half of each specimen's width approximately. Each specimen was imaged in SE mode (a, c) and in BSD mode (b, d). White dotted lines indicate the final front of the fatigue precracks.

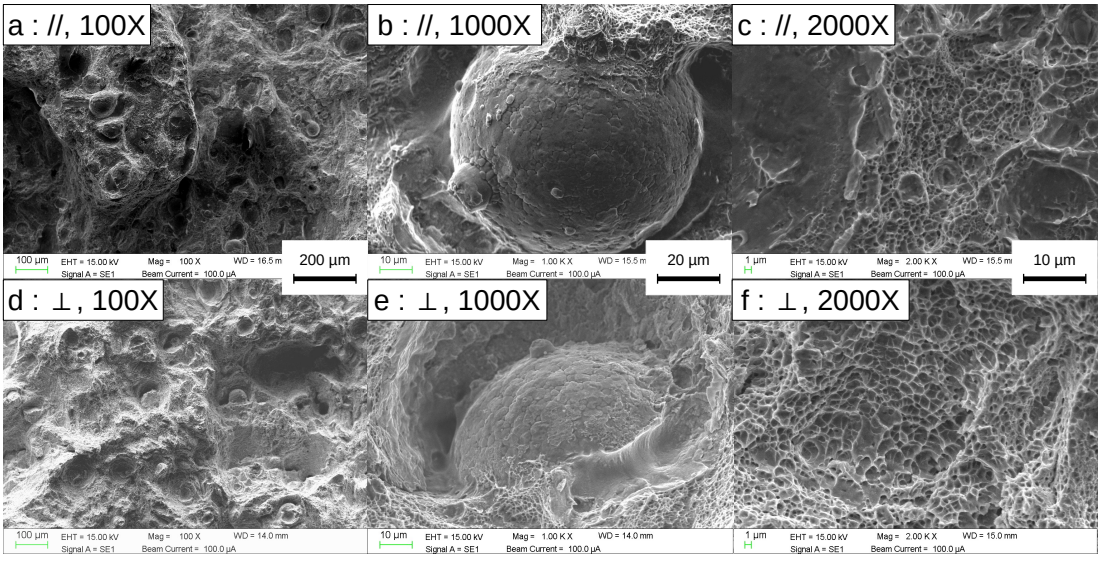

Figure 10: SEM observations of the crack surface near the fatigue precrack for a // specimen (a, b, c) and a ⊥ specimen (d, e, f). (a, d) : General aspect of the crack surfaces at 100X magnification. (b, e) : Unmelted or semi-melted powder particles. (c, f) : Microvoid coalescence dimples. The three image couples each share the same scales. All images were taken in SE mode. The reader is invited to consult the online supplemental material for more SEM pictures and their locations within the crack surface.

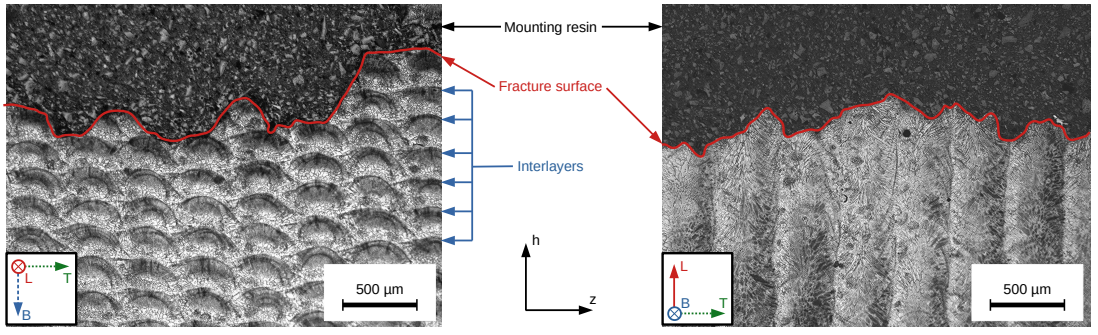

Figure 11: Optical microscope observation of a section orthogonal to the fracture surface for a // specimen (left) and a ⊥ specimen (right), after electrolytic etching with 10% oxalic acid. The crack propagation direction was along the out-of-plane axis in both cases. The (z-h) axis system refers to the roughness analysis in §4.3.2.

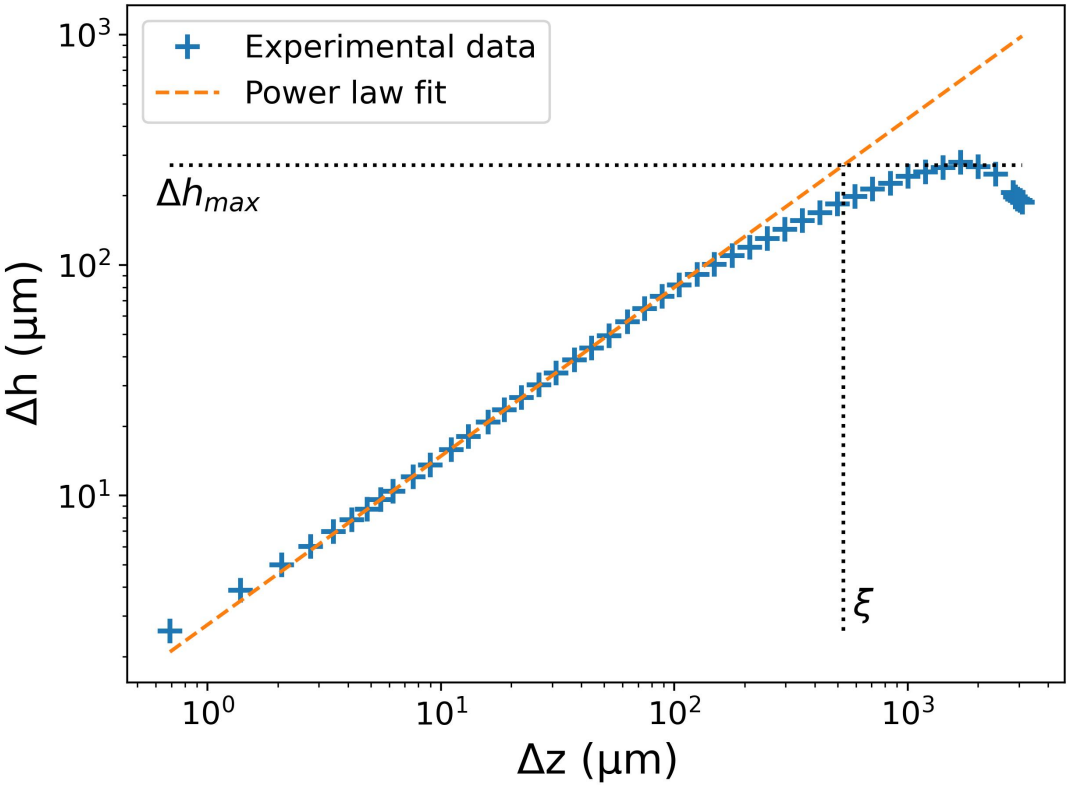

Figure 12: Height-height correlation function Δh obtained for the // orientation. The hashed line represents the power law fit.

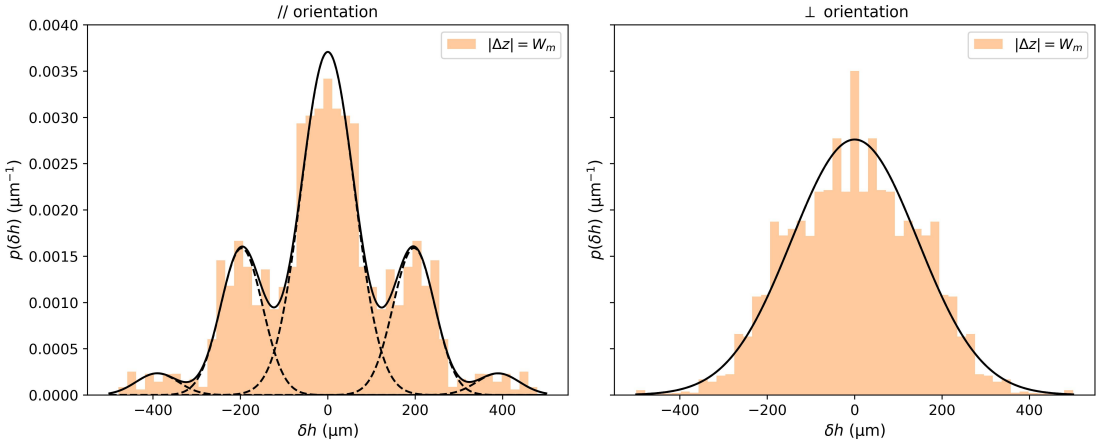

Figure 13: Probability densities of the $\delta h(z, \Delta z)$ values for $|\Delta z| = W_m$ and fitted models. Left : // orientation fitted with a five component Gaussian Mixture Model. Each individual Gaussian is shown as a dotted line, and the continuous line represents the total mixture. Right : ⊥ orientation fitted with a single Gaussian curve.

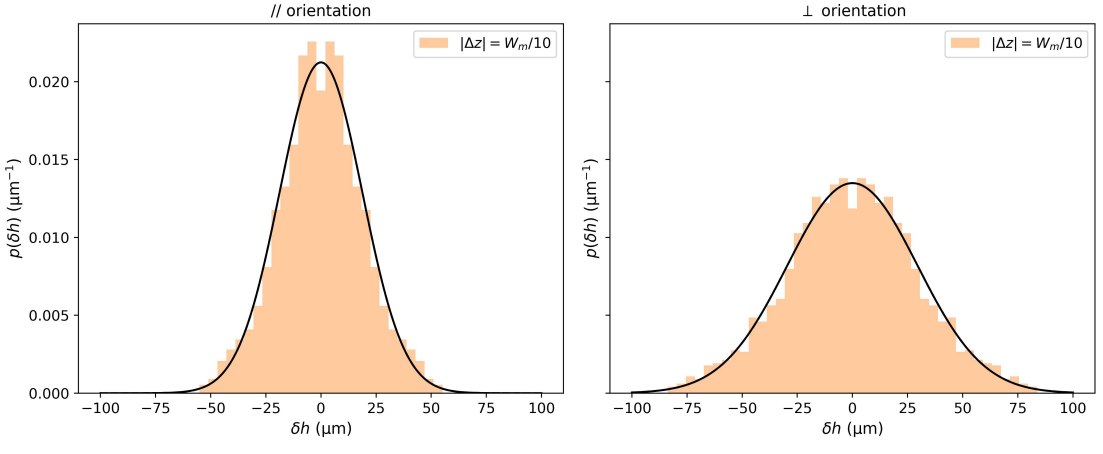

Figure 14: Probability densities of the $\delta h(z, \Delta z)$ values for $|\Delta z| = W_m/10$ and fitted models. Left : // orientation fitted with a single Gaussian curve. Right : ⊥ orientation fitted with a single Gaussian curve.

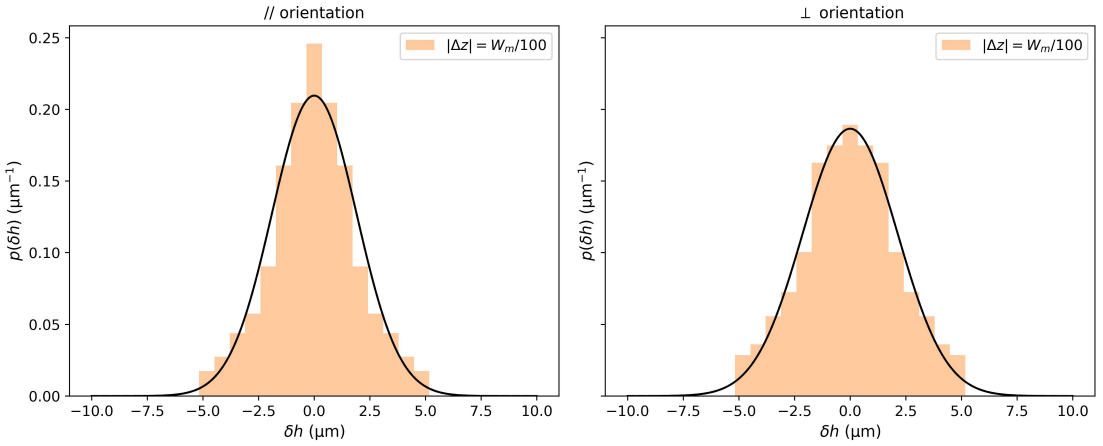

Figure 15: Probability densities of the $\delta h(z, \Delta z)$ values for $|\Delta z| = W_m/100$ and fitted models. Left : // orientation fitted with a single Gaussian curve. Right : ⊥ orientation fitted with a single Gaussian curve.

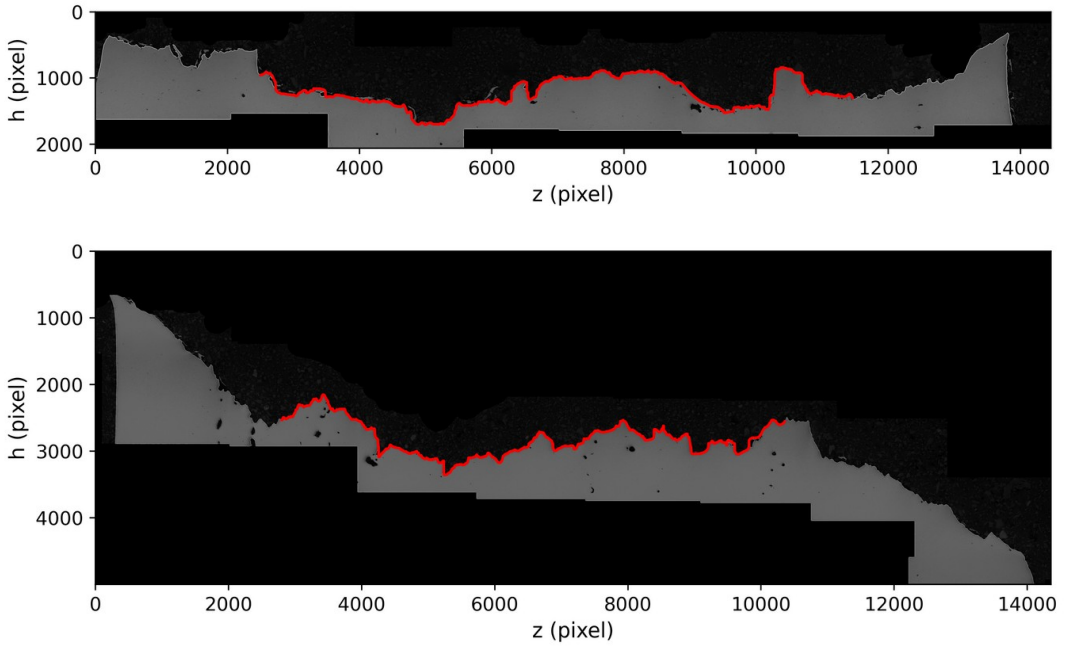

Figure 16: Images of studied faces after re-polishing for the // (top) and ⊥ (bottom) orientation. Only one of the two studied faces for each orientation is presented here. The red lines represent the detected profiles.

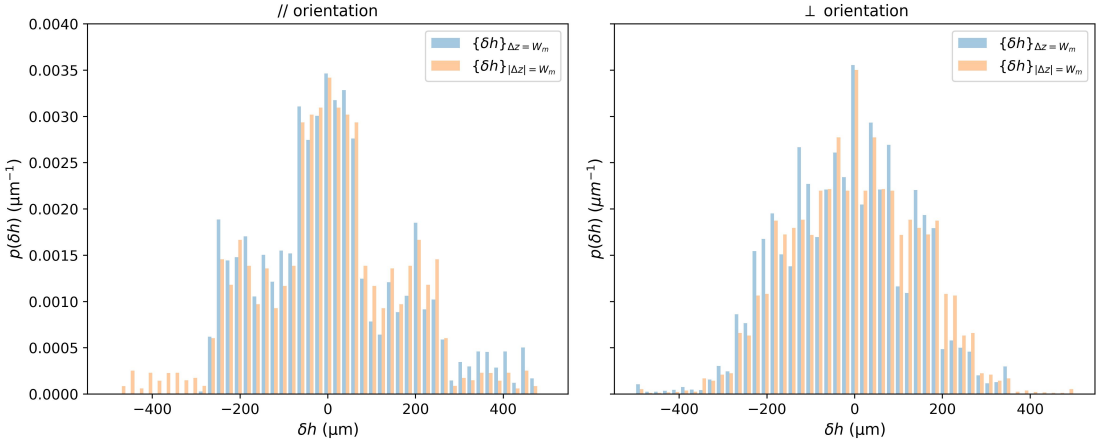

Figure 17: Histograms representing the probability densities of the $\delta h(z, \Delta z)$ values, over 50 bins. The blue histograms correspond to the sets $\{\delta h\}_{\Delta z = W_m}$ and the orange histograms represent the supersets $\{\delta h\}_{|\Delta z| = W_m}$. Left : // orientation. Right : ⊥ orientation.

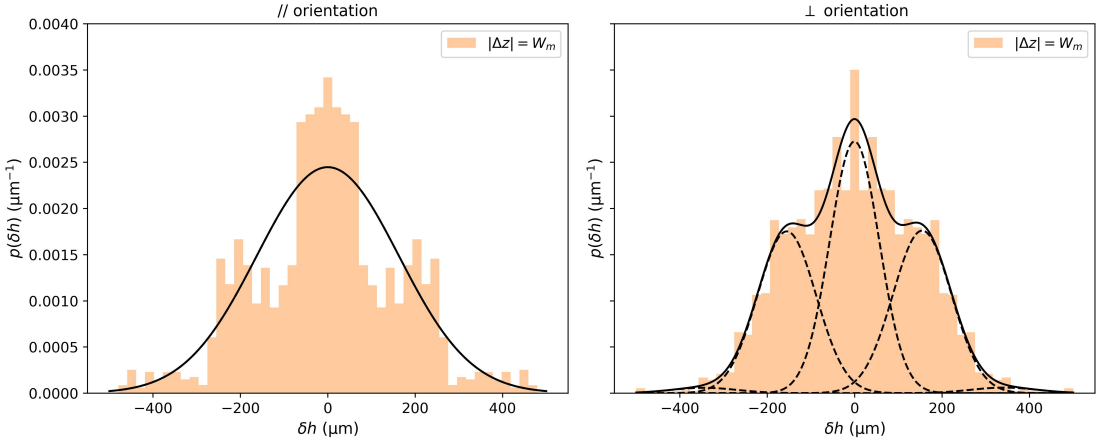

Figure 18: Probability densities of the $\delta h(z, \Delta z)$ values for $|\Delta z| = W_m$ with swapped fitting models. Left : // orientation fitted with a single Gaussian curve. Right : ⊥ orientation fitted with a five component Gaussian Mixture Model. Each individual Gaussian is shown as a dotted line, and the continuous line represents the total mixture.